The CO2Image mission: retrieval studies and performance analysis

Philipp Hochstaffl, *Remote Sensing Technology Institute (IMF), German Aerospace Center (DLR)*, Oberpfaffenhofen, Germany
Email: philipp.hochstaffl@dlr.de

Andreas Baumgartner, *IMF, DLR*, Oberpfaffenhofen, Germany
Franz Schreier, *IMF, DLR*, Oberpfaffenhofen, Germany
Claas H. Köhler, *IMF, DLR*, Oberpfaffenhofen, Germany
Sander Slijkhuis, *IMF, DLR*, Oberpfaffenhofen, Germany
Günter Lichtenberg, *IMF, DLR*, Oberpfaffenhofen, Germany
Thomas Trautmann, *IMF, DLR*, Oberpfaffenhofen, Germany
Anke Roiger, *Institute of Atmospheric Physics (IPA), DLR*, Oberpfaffenhofen, Germany
Dietrich G. Feist, *IPA, DLR*, Oberpfaffenhofen, Germany
Julia Marshall, *IPA, DLR*, Oberpfaffenhofen, Germany
André Butz, *Institute of Environmental Physics (IUP), University of Heidelberg*, Germany

***Abstract*—The CO2Image satellite mission, led by the German Aerospace Center (DLR), aims to demonstrate the feasibility of quantifying carbon dioxide (CO_2) and methane (CH_4) emissions from medium-size point sources. Several DLR institutes are currently working on the preliminary design phase (Phase B) of the mission. Here we present a performance analysis based on the current instrument specifications. The Beer InfraRed Retrieval Algorithm (BIRRA), the line-by-line radiative transfer model Py4CAtS (Python for Computational ATmospheric Spectroscopy) and a COSIS (Carbon dioxide Sensing Imaging Spectrometer) instrument model are employed to infer CO_2 and CH_4 concentrations from synthetic COSIS spectra. We evaluate the instrument's performance and determine if it meets the intended requirements. The study assesses uncertainties in the retrieved concentrations as well as errors in point source emission estimates caused by instrument noise. First results suggest that the detection and quantification limits stated in the mission requirements document are justified. The analysis also demonstrates that retrieval errors tend to increase when the signal-to-noise ratio is low, complicating the distinction between emission sources and background concentrations. Furthermore, we discuss non-instrumental effects and demonstrate that the fit quality significantly improves if a low-level plume is scaled instead of a background reference profile that covers the atmosphere's full vertical extent. The analysis on heterogeneous scenes (high albedo contrast) reveals that the various instrument setups perform similarly for both molecules.**

***Index Terms*—carbon dioxide, methane, concentration fields, emission rates, short-wave infrared, radiative transfer, inversion**

I. Introduction

Carbon dioxide (CO_2) is a crucial component of the Earth's atmosphere that helps to regulate our planet's climate. However, human activities have caused a significant increase in atmospheric CO_2 levels, leading to climate change. Methane (CH_4) is an even more potent greenhouse gas with a global warming potential over 25 times higher than CO_2 over a 100-year time frame. Understanding the sources and dynamics of both atmospheric constituents is vital for developing effective strategies to mitigate the impacts of climate change [1].

In this context the United Nations Framework Convention on Climate Change (UNFCCC) requires countries to report their greenhouse gas emissions, including carbon dioxide. Independent verification of these reported emissions is essential for accounting and effective reduction measures, as outlined in the Paris climate agreement [2]. However, currently there is no global independent emission verification system in place. Although planned satellite missions such as the European Carbon Constellation (CO2M, [3]) will monitor global emissions, their focus is on large urban agglomerations (>Berlin) and isolated large power plants (>10 MtCO2/yr), leaving a significant fraction of the total emissions unaccounted for.

CO2Image is a demonstrator satellite mission envisioned to complement global survey missions as a magnifying glass to zoom in on sources. The platform is intended to fly in a sun-synchronous low earth orbit at between 525 km and 575 km, with a local overpass time of about 10:30. The national mission is led by the German Aerospace Center (DLR) and was originally planned to launch in 2026.

The primary mission objective is to demonstrate the feasibility of quantifying carbon dioxide emissions from localized sources such as coal-fired power plants down to medium source strength >1 Mt/yr (with detection above 0.3 Mt/yr). Column-integrated atmospheric CO_2 enhancements from the local background (ΔXCO_2) shall be measured with a precision of 2 ppm (or better) for a dark reference scene ($1.0 \cdot 10^{12}$ photons/s/nm/cm^2/sr). Point source emissions will be derived from the gradients in XCO_2 relative to the local background. The secondary mission objective is to quantify methane emissions from localized sources such as oil/gas facilities and

TABLE I
SUMMARY OF SOME IMPORTANT COSIS INSTRUMENT PROPERTIES.

Property	Value
Mass	110 kg
Swath	50 km
Spatial resolution	50 m×50 m
Spectral range	1950–2400 nm
FWHM (2.5 pix)	1.29 nm
Resolving power	1600
Aperture diameter	15.0 cm
f number	2.4
Integration time	70 ms

landfills down to source strength >300 kg/hr (with detection above 100 kg/hr).

Localized CO_2 emission monitoring poses some significant challenges, such as the need for a sufficient ground resolution to accurately detect and resolve plumes in specific locations [4]. This requirement often comes at the expense of decreasing the spectral resolution of the instrument. The COSIS (Carbon dioxide Sensing Imaging Spectrometer) instrument aboard the CO2Image platform observes reflected solar radiation in the Short-Wave InfraRed (SWIR) from 1950–2400 nm where molecular absorption allows to infer molecular concentrations of CO_2 and CH_4 in the atmosphere. Moreover, SWIR observations have a sensitivity that extends down to the tropospheric boundary layer. The moderate spectral resolution of 1.30 nm at FWHM (Full Width Half Maximum) is optimized to maximize signal strength while minimizing correlations with the surface spectral reflectance [5]. The high spatial resolution of 50 m×50 m requires to employ a "staring" technique where COSIS looks at each along-track row of measurements and adjusts the viewing angle as it flies, using forward-motion compensation. The downside of this method is that the instrument proceeds nearly 700 km during the observations over a single 50 km×50 km target area. Due to the additional time required for repositioning and stabilization, the satellite can only select five to seven targets from the daytime side per orbit. A list of some basic instrument parameters is given in Table I.

II. METHODOLOGY

A. Radiative transfer and inversion

In atmospheric remote sensing the forward model $F(\boldsymbol{x}, \boldsymbol{b}, \lambda)$ is represented by a radiative transfer model that mimics the observed measurements based on a given set of input parameters. In order to retrieve atmospheric gas concentrations such as carbon dioxide and methane, an inverse method is employed to find (retrieve) values that best match the observed measurements.

B. Forward modelling

Line-by-line models rely on high-resolution molecular spectroscopy data to calculate the absorption of radiation by atmospheric constituents such as water vapor (H_2O), CO_2, and CH_4 (see Fig. 1). Moreover, these models require atmospheric pressure, temperature, composition to accurately calculate molecular optical depths.

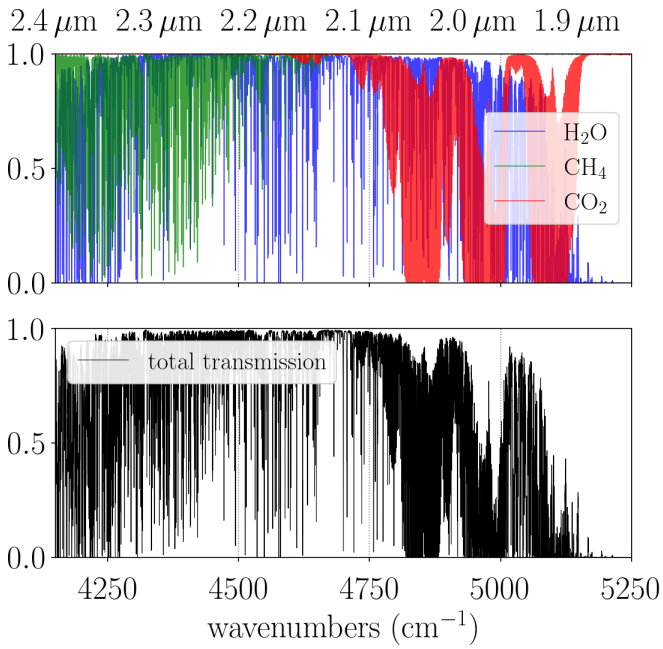

Fig. 1. Exemplary monochromatic transmissions in the SWIR spectral range for a nadir looking observer.

In the SWIR spectral range the upwelling radiance observed by a nadir looking space-borne observer under clear sky conditions is described by Bouguer-Beer's law according to

$$F(\boldsymbol{x}, \boldsymbol{b}, \lambda) = \frac{r(\lambda)}{\pi} \cos(\theta)\, E_{\text{sun}}(\lambda) \exp\left(- \int_{\text{path}} \sum_m \alpha_m \tau_m \right) \otimes \mathcal{S}(\lambda, \gamma)\,, \quad (1)$$

where r refers to the surface reflectivity, E_{sun} the irradiance at top-of-atmosphere and θ represents the solar zenith angle. The model assumes a pure gas atmosphere with the optical depth τ_m given by the path integral over the molecular number densities n_m and the pressure and temperature dependent absorption cross section k_m

$$\tau_m = \int_{\text{path}} \mathrm{d}s \sum_m n_m(s)\, k_m(\lambda, p(s), T(s))\,. \quad (2)$$

The unknown (to be estimated) parameters are composed as elements of the state vector $\boldsymbol{x}$ which includes, e.g., the molecular scaling factors α_m of the individual molecules m that scale the initial guess profiles. The instrument spectral response (ISRF) to the monochromatic at-aperture radiance is either modelled by the convolution $\mathcal{S} = \text{Gauß} \circledast \text{Box}$ or read from tabulated values.

C. Retrieval

Fitting the model in Eq. (1) to some observation $\boldsymbol{y}_{\text{obs}}$ by nonlinear least squares is accomplished by finding the minimum 2-norm of the objective function with respect to $\boldsymbol{x}$

$$\min_{\boldsymbol{x}} \left\| \boldsymbol{y}_{\text{obs}} - \boldsymbol{F}(\boldsymbol{x}, \boldsymbol{b}) \right\|^2 . \quad (3)$$

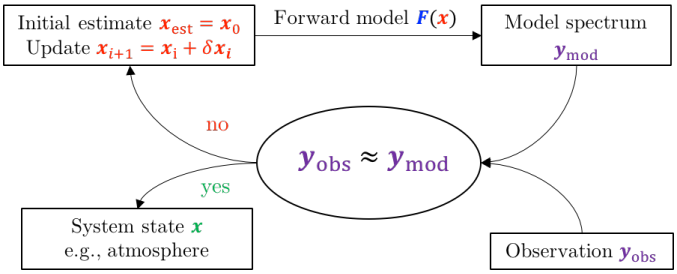

Fig. 2. Schematic depiction of an iterative optimization algorithm. The number of iterations is influenced by the tolerance criteria $|\Delta \boldsymbol{x}| \,/\, |\boldsymbol{x}| < \varepsilon_x$ and $|\boldsymbol{y}_{\text{obs}} - \boldsymbol{y}_{\text{mod}}| < \varepsilon_y$ [9, Fig. 3.2].

The vector $\boldsymbol{b}$ comprises all model parameters required by the forward model that are not retrieved by the inversion, i.e. geometry, p, T, molecular optical properties such as line data, etc. Nonlinear least squares methods are iterative (see Fig. 2) and require calculating derivatives for each of the state vector elements across the spectral axis $\nabla_{\boldsymbol{x}} F(\boldsymbol{x}, \boldsymbol{b})$, starting from the initial guess $\boldsymbol{x}_0$.

In this study the new Python version of the BIRRA (Beer InfraRed Retrieval Algorithm, [6], [7]) level 2 processor is used for the retrieval of column-averaged mole fractions X_m (i.e., XCO_2 or XCH_4). The spectral interval for the retrieval is 1950–2450 nm. The code employs Py4CAtS (Python for Computational Atmospheric Spectroscopy, [8]) as its forward model which together comprise a flexible toolbox for prototyping.

D. Python for Computational Atmospheric Spectroscopy

The Py4CAtS software package is a Python reimplementation of the Fortran Generic Atmospheric Radiation Line-by-line Code (GARLIC, [10]) and is publicly available under the link https://atmos.eoc.dlr.de/tools/Py4CAtS/index.html. In Py4CAtS the individual steps of a IR computation are implemented in separate modules and functions which are sketched in Fig. 3. The calculation of absorption cross sections by `lbl2xs` is the computationally most demanding step. This study exploits GEISA 2020 (Gestion et Etude des Informations Spectroscopiques Atmosph'eriques; [11]) spectroscopic line data to compute the molecular absorption cross sections but HITRAN (HIgh resolution TRANsmission database, [12]) can be used alternatively. The sum of all cross sections scaled by the molecules number densities gives the absorption coefficient (ac). This step (including appropriate interpolation) is performed by the `xs2ac` function level-by-level. Next the absorption coefficients are integrated by `ac2dod` to compute the vertical delta (or layer) optical depths (dod) — the result is

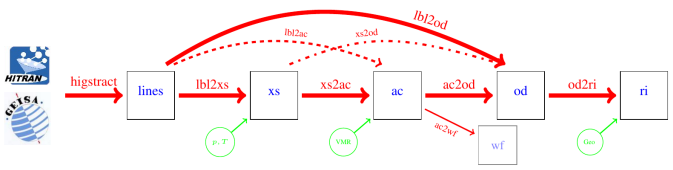

Fig. 3. Individual steps of a SWIR computation in Py4CAtS.

a list of optical depths, one for each atmospheric layer (defined by the lower and upper levels).

Usually, the steps `lbl2xs`, `xs2ac`, and `ac2dod` are completed at once by the function `lbl2od`. Finally, `dod2tod` is used to calculate the total optical depth by summing up all layer optical depths, which is the integral of the absorption coefficient from bottom- to top-of-atmosphere. To avoid time-consuming recomputing of `lbl2xs` precomputed optical depths were saved via `odSave` and then read by `odRead`.

E. Spectrum generation and Level-2 processing

In order to test and evaluate the performance of retrievals, synthetic COSIS spectra from 1950–2450 nm (Level-1b data) must be created for a set of scenes. First, high-resolution at-aperture radiance spectra for perturbed molecular concentration profiles are generated using Py4CAtS. To generate representative signal and noise levels, the total instrument signal is derived and COSIS radiometric calibration is applied. Note that the instrument noise is caused by several factors, which include calibration errors, detector noise, and background noise. Finally, the signal is converted back to spectral radiance at instrument resolution (sampling 0.65 nm) and XCO_2 and XCH_4 are then retrieved from the Level-1b radiance data (see Fig. 4) using BIRRA.

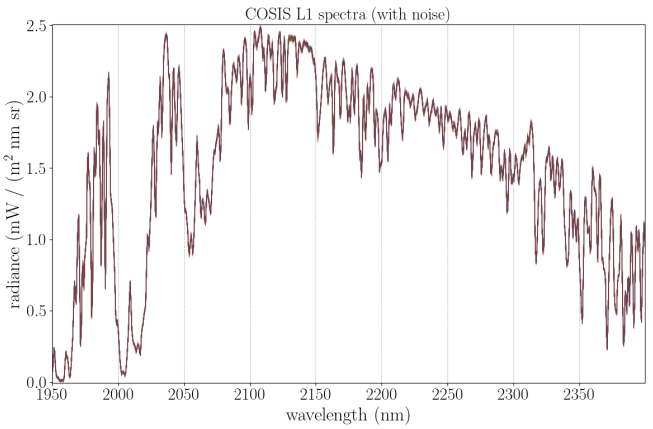

Fig. 4. Example of 100 noisy COSIS Level-1b radiance spectra for scene with 30 % surface reflectivity and US-Standard atmospheric conditions [13], except for CO_2 and CH_4 concentration profiles, which were scaled to 410 ppm and 1785 ppb, respectively.

III. Results

A. Signal to noise impact

The primary objective is to assess the impact of instrument noise on the retrieval errors of CO_2 and CH_4. Therefore, the effect on the retrieval's accuracy and precision is evaluated for different surface albedos and concentration enhancements. The results of this analysis will provide insight into the sensitivity of the retrieval to signal-to-noise (SNR), which is a crucial aspect in the preliminary design phase of the mission.

Figure 5 depicts the difference between the retrieved and true molecular concentration as a function of the albedo. The retrieval ensemble comprises 4000 observations ranging from

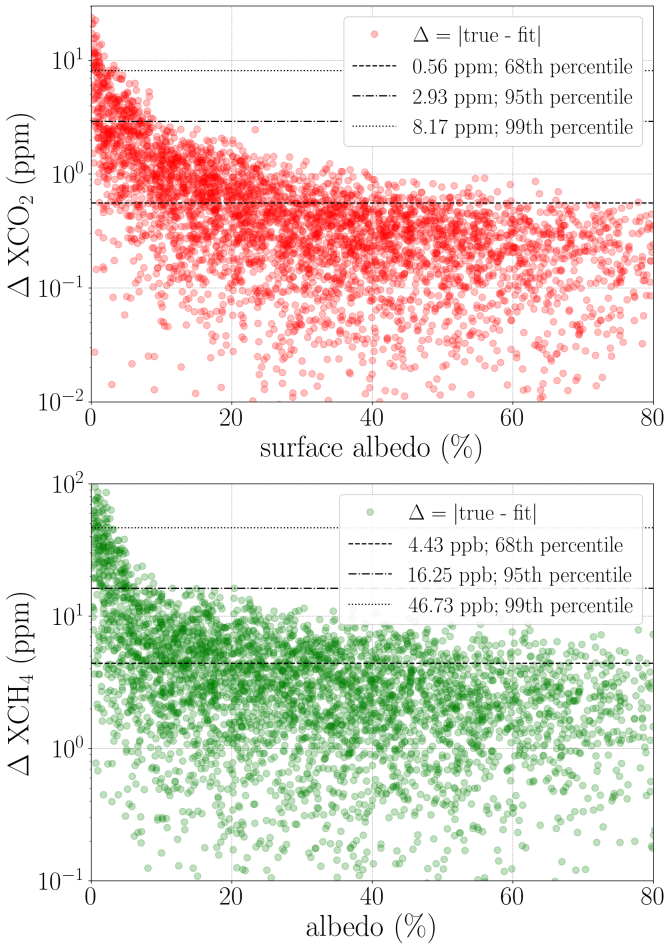

Fig. 5. Noise errors as a function of surface brightness, with the dotted line indicating our reference scene and the dashed lines indicating the 68th and 95th percentiles of the XCO_2 and XCH_4 noise errors for the different spectral setups.

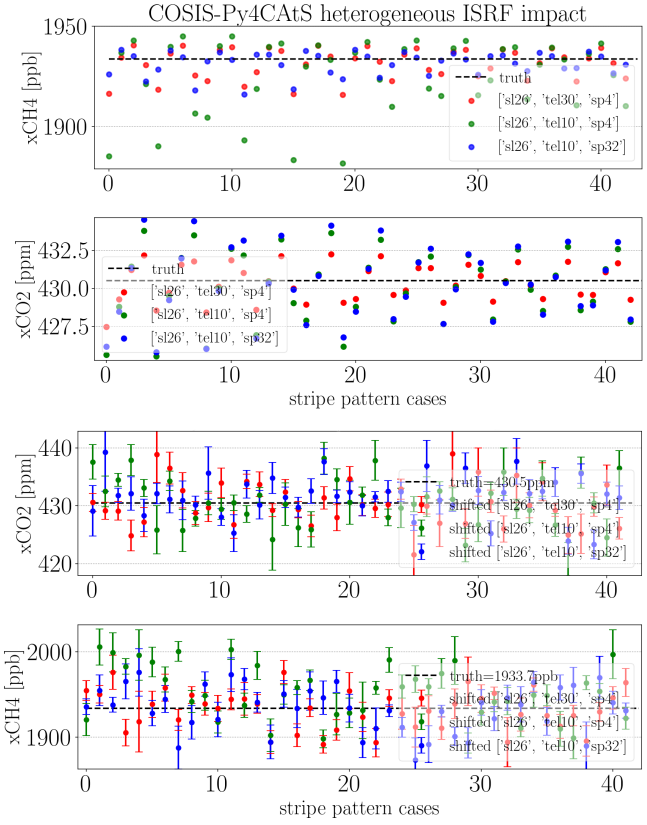

Fig. 6. Systematic deviations of fitted CO_2 and CH_4 caused by the model error due to non-homogeneous illumination of the instrument slit for a given molecular enhancement. The impact is shown for different "blur functions". The top panels shows the outcome for noise-free spectra while in the lower panels noisy COSIS spectra with shifted ISRFs were fitted.

0–15 ppm (CO_2) and 0–50 ppb (CH_4). Most fits show good agreement and large retrieval errors are associated with low SNR values which are typically attributed to observations over dark surfaces. It was found that the CO_2 estimates have a higher correlation with the true values (R^2=0.80) compared to CH_4 (R^2=0.54). However, this is expected as the examined CH_4 enhancements are closer to the detection limit (see Sec. I). For CO_2 the results indicate that the retrieval error is within the requirement of <2 ppm for surfaces that reflect approximately >10 % of the incident intensity. A similar conclusion can be drawn for the CH_4 fits which yield precisions <10 ppb for albedos approximately >20 %.

B. Impact of heterogeneous scene albedo

The aim is to evaluate the impact of heterogeneous albedos (light/dark patterns) within a COSIS pixel on the retrieval of CO_2 and CH_4. Heterogeneous albedos can cause non-uniform illumination of the instrument slit, which distorts the Spectral Response Function (ISRF) and hence induces a model error. The effect is examined for extreme contrasts (5 % to 85 %) and for more realistic scenes (10 % to 50 %). The stripe pattern is slightly displaced with each measurement, resulting in a shifted light/dark boundary for the 43 examined cases.

The effective ISRF for a given albedo pattern is computed, and the impact of the gradient in brightness across the pixel is analyzed for different blur functions of the instrument components: telescope (front optics), slit, and spectrometer. The nominal COSIS setup is sl26-tel10-sp4 (Variant B, green), where the numbers indicate the respective widths in μm. By combining the three variants, a different blur effect is produced, which affects the intensity gradient across the slit width.

To quantify the impact on the fit, the retrieval assumes a homogeneous scene and convolves the high-resolution Py4CAtS spectrum using the nominal COSIS response function, while the COSIS spectra are generated with the distorted ISRF according to the simulation. The results for the heterogeneous scene fits are shown in Figure 6. All setups perform similarly with respect to CO_2, while Variant B (nominal) shows slightly larger deviations for CH_4. However, the retrieval results indicate no significant difference between spatial and spectral smearing.

C. Vertical concentration profiles

This section examines the impact of different vertical concentration profiles on the total column fit. The column-

integrated mole fractions of the target gas are composed of a background and a plume component. While the background is taken from the US-Standard atmosphere, the plume component is modeled with a triangle or Gaussian at a specified altitude and half width (see Fig. 7). Since the emissions that are targeted by the CO2Image are located close to the ground with molecular enhancements likely remaining within the planetary boundary layer in the vicinity of the source, only the plume component should be varied. In order to quantify the error caused by scaling a wrong vertical concentration profile, COSIS spectra are generated with molecular number densities that do not match the initial guess profiles, resulting in a model null-space error.

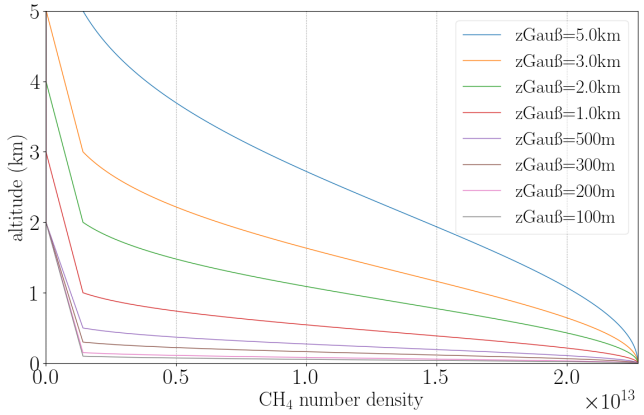

Fig. 7. An ensemble of low-level Gaussian shaped plume profiles that are available in the profile scaling BIRRA retrieval.

Fig. 8 (top panel) shows the retrieval result for a background profile fit of a low-level triangle shaped plume (truth) of CO_2 (left) and CH_4 (right). The error for the background profile fit increases with concentration enhancements and is found to be roughly 1 % and 0.5 % for realistic low-level plume number densities of CO_2 and CH_4, respectively. Note that the induced offset is positive for the former and negative for the latter molecule. In the lower panel a Gaussian plume profile according to Fig. 7 was employed. The results show that the fit quality improves significantly, roughly two to three-fold for realistic enhancements.

D. Gaussian plumes

In order to estimate the retrieved enhancements from given point source emissions a Gaussian plume model is employed. The model calculates the concentration enhancement field $X_{\mathrm{pl}}(x, y, z)$ of a substance for a constant emission rate E from a source located at (x_0, y_0, z_0), wind speed u_0 in x-direction, and atmospheric stability σ according to

$$X_{\mathrm{pl}}(x,y,z) = \frac{E(x_0,y_0,z_0)}{2\pi\, u_0\, \sigma_y(x)\, \sigma_z(x)} \exp\left(-\frac{(y-y_0)^2}{2\sigma_y^2(x)}\right) \exp\left(-\frac{(z-z_0)^2}{2\sigma_z^2(x)}\right) . \quad (4)$$

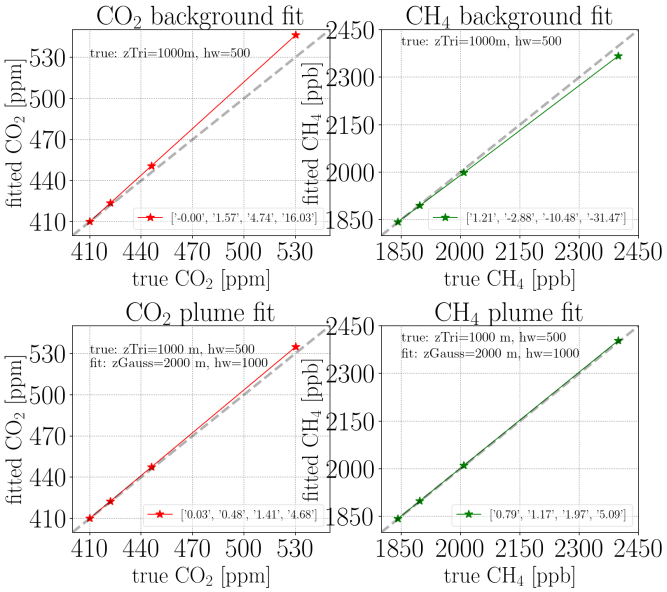

Fig. 8. Impact of vertical concentration profiles on the fit quality for a reference scene with 30 % albedo. Synthetic measurement are generated with a triangle shaped plume at 1000 m with a half width of 500 m.

The equation describes a mixing process that results in a Gaussian concentration distribution both in crosswind and in the vertical directions, centered at the line downwind from the source. The standard deviations of the distribution, $\sigma_y(x)$ and $\sigma_z(x)$, represent the plume's spread in the y and z-directions and is given by the turbulent diffusion coefficients

$$\sigma_{y,z}(x) = \sqrt{2\, K_{y,z}\, \frac{x}{u_0}} , \quad (5)$$

where K_y=40 m^2/s, and K_z=10 m^2/s represent rather typical values in the lower troposphere. Note that the plume's spread increases with distance from the source.

The simulations are performed for a model domain of (10 km, 1 km, 100 km) with a native model resolution of (5 m, 5 m, 10 m) in the x, y, and z directions. Five sources with stack heights between 10 m and 100 m, and emission rates close to the quantification and detection limits are added. Subsequently, the model output is convolved with a box that mimics COSIS's 50 m×50 m ground resolution. A surface albedo chart is added to generate synthetic spectra according to Sec. II-E.

Single overpass retrieval output for the 10 km×1 km scene is illustrated in Fig. 9. The top panel depicts the vertically integrated CO_2 mole fractions while the corresponding CH_4 concentrations are shown below. The plumes are characterized by an enhancement relative to the local background. The elevated concentrations downwind are well captured with noise levels primarily depending on the surface reflectivity (also see Fig. 5).

The frequency distribution of mole fractions is shown in Fig. 10. The figure depicts the single and averaged retrieval output for ten overpasses together with the true values. The low frequency of XCO_2 and XCH_4 for pixels with close to zero enhancements is caused by the retrieval noise which yields negative values for some of those observations. However, note

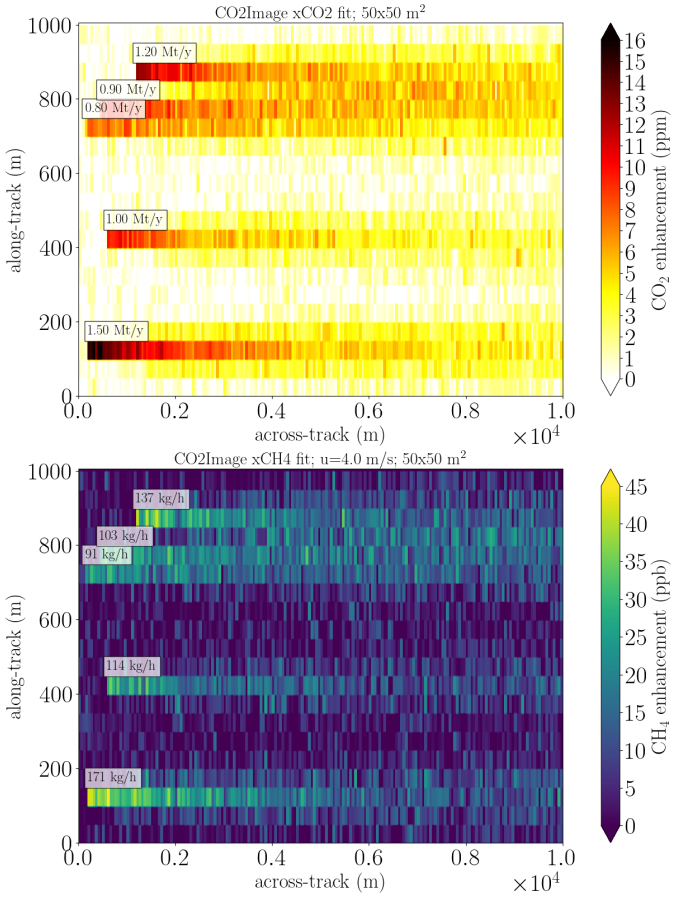

Fig. 9. Retrieval output for concentrations fields ΔX from five point-like sources with various emission rates. Wind speed u_0=4 m/s. Note that the CH_4 emissions are close to the detection limit while CO_2 sources are emitting around the quantification limit.

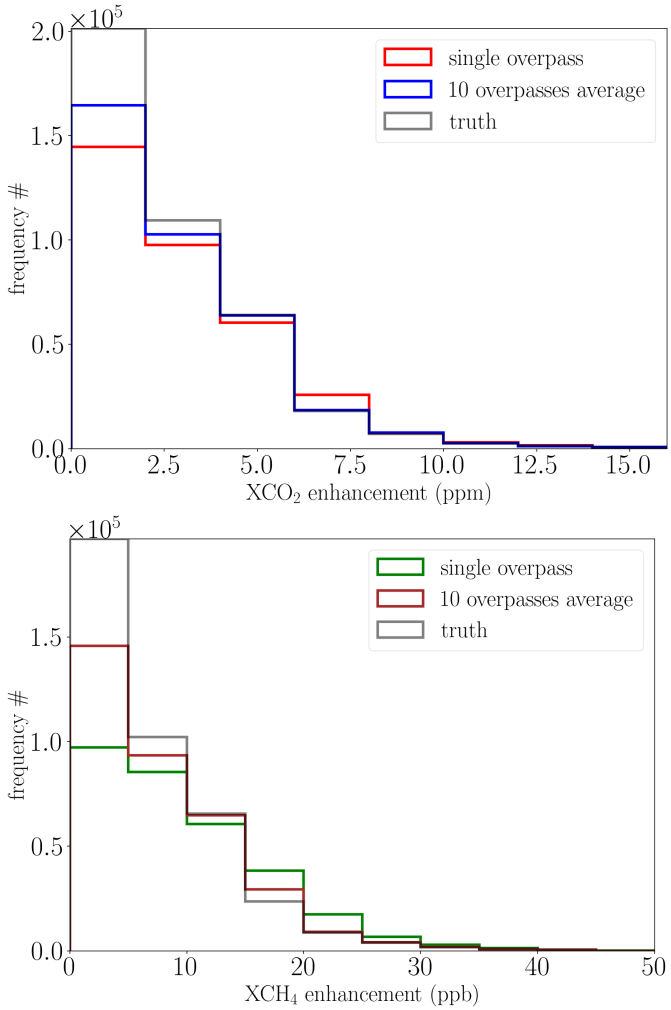

Fig. 10. Histogram of fitted CO_2 (top) and CH_4 (below) enhancements from a scene with point-like emissions according to Fig. 9. The true value represents the Gaussian model output without any retrieval applied.

that this error is reduced in the averaged output, leading to a smoother distribution of values that is closer to the truth.

E. Emission estimates

In order to compute the source rate E from column-averaged mole fractions X the inferred concentration enhancement $\Delta X = X - X_{\mathrm{bg}}$ is expressed as the column mass enhancement

$$\Delta\Omega = \frac{M_m}{M_{\mathrm{air}}}\,\Omega_{\mathrm{air}}\,\Delta X_m\,, \tag{6}$$

where M_m and M_{air} are the molar masses of molecule m and dry air, respectively, and Ω_{air} is the column of dry air.

Various methods have been used in the past to quantify point source emission rates from plume observations [14]–[16]. In this study we employ the cross-sectional flux method (XSFM) where the source rate E is estimated by computing the flux through one or more cross sections orthogonal to the plume axis. Figure 11 depicts the setup with transects along the y axis perpendicular to the wind. By mass balance, the source rate E must be equal to the product of the wind speed and the column plume

$$E = \int_{-\infty}^{\infty} u_0(x,y)\,\Delta\Omega(x,y)dy\,, \tag{7}$$

where the integral is approximated in the observations as a discrete summation of the product $u_0(x,y)\Delta\Omega(x,y)$ over the detectable width of the plume. Since a single transect suffers from noise the average cross-sectional flux is computed (using two to five transects). Note that in Eq. (7) we assume the model wind u_0 to be equal to the effective wind. The latter is used to describe a vertical average wind speed over the plume extend which is required in real world scenarios or LES (Large Eddy Simulations, [14, Sec. 6]).

TABLE II
EMISSION RATE ESTIMATES VIA THE XSFM FOR A SINGLE CO_2 SOURCE. UNCERTAINTIES ARE CAUSED BY INSTRUMENT NOISE.

Albedo (%)	**CO_2 emission rates** E (Mt/yr)		
$N(\mu,\sigma)$	5	1 (QL)	0.3 (DL)
$N(50,20)$	±.08 (≈1.5%)	±.09 (≈10%)	±.09 (≈30%)
$N(30,20)$	±.24 (≈5%)	±.29 (≈30%)	±.21 (≈70%)
$N(10,10)$	±.43 (≈10%)	±.48 (≈50%)	±.45 (≈150%)

Table II and III present the outcome of estimated emissions E based on mass concentration enhancements $\Delta\Omega$ inferred from synthetic COSIS observations. The analysis is conducted

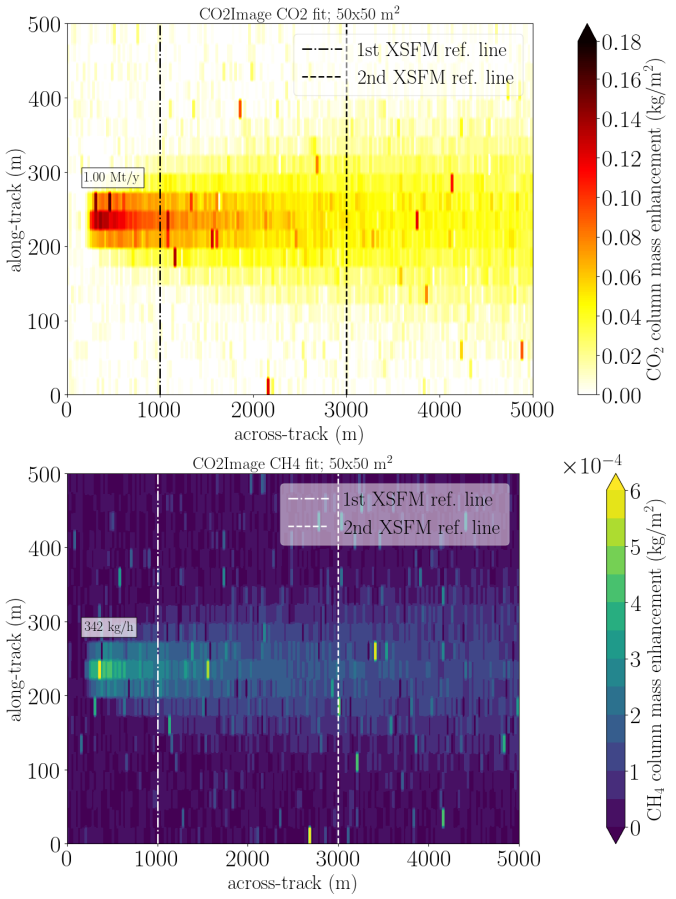

Fig. 11. Enhancements in mass concentration of CO_2 and CH_4 for a source emitting at the anticipated COSIS quantification limit (QL). The downwind transects used for the emission estimates are marked by black and white dashed lines.

for three distinct albedo maps and varying source strengths. The data reveal a trend towards larger absolute errors as albedo levels decrease, but no significant dependence on the source strength and hence the magnitude of enhancement. Consequently, relative errors increase towards lower column mass enhancements over a given scene. The table indicates that instrument noise alone is responsible for ≈10%–50% of the uncertainty in the emission rates at the specified quantification limit (QL). It is found that distinction of the source from background becomes unfeasible for low albedo scenes at the detection limit (DL). Based on these findings the QL and DL in the mission requirements document seem to be reasonable and justified.

TABLE III
ESTIMATES OF CH_4 SOURCE STRENGTH WITH THE XSFM.

Albedo (%)	**CH_4 emission rates** E (kg/hr)		
$N(\mu, \sigma)$	500	300 (QL)	100 (DL)
$N(50, 20)$	±30 (≈5%)	±25 (≈10%)	±35 (≈35%)
$N(30, 20)$	±60 (≈10%)	±55 (≈20%)	±65 (≈65%)
$N(10, 10)$	±155 (≈30%)	±160 (≈55%)	±130 (≈150%)

IV. CONCLUSIONS

The study evaluates the expected COSIS performance for the CO_2 and CH_4 estimates and discusses non-instrumental effects. The investigations are conducted as part of the preliminary design phase of the CO2Image mission.

The SNR analysis in Sec. III-A showed that large retrieval errors were associated with low SNR values over dark surfaces. It is worth noting that low SNR or albedos do not introduce any systematic bias to the retrieved quantities. If the number of samples is sufficiently high, the mean matches the truth. Overall, the retrieval errors were within requirements for specific albedo ranges for both gases.

The analysis on heterogeneous scenes in Sec. III-B examined the impact of the gradient in brightness within a COSIS pixel on the ISRF for different instrument setups and found that the setups perform similarly with respect to CO_2, but there were slightly larger deviations for CH_4.

The investigations in Sec. III-C studied the impact of different vertical concentration profiles on the total column fit and found that the fit quality improves two to three-fold for realistic enhancement values when a low-level plume is scaled instead of the US-Standard background reference profile.

The paragraphs in Sec. III-D describe the retrieval output for a Gaussian plumes scene. The results reveal that single overpass fits show noise levels in accordance with findings in Sec. III-A while averaging the retrieval output for multiple overpasses yields a smoother distribution of enhancements that is in better agreement with the truth.

In Sec. III-E uncertainties in the emission estimates caused by instrument noise are presented. It is found that COSIS noise accounts for a significant fraction of uncertainty, ranging up to 50% for low albedo scenes at the QL. A noteworthy observation is also the increase in absolute errors with decreasing albedo levels, which poses challenges for emission quantification in low albedo environments (Central Europe?!). The results find that discerning the emission source from background concentrations becomes increasingly difficult at the currently defined DL in low albedo scenes. To put the result into perspective the photon flux specified for the quantification limits in Sec. I corresponds to a radiance of ≈1.0 at 2100 nm when converted to units given in Fig. 4.

The results shown in this report represent an overview of the current state. As we continue to conduct further research and analysis, the findings may evolve and be updated in future publications accordingly.

REFERENCES

[1] IPCC, "Summary for policymakers," in *Climate Change 2021: The Physical Science Basis. Contribution of Working Group I to the Sixth Assessment Report of the Intergovernmental Panel on Climate Change*, V. Masson-Delmotte, P. Zhai, A. Pirani, S. Connors, C. Péan, S. Berger, N. Caud, Y. Chen, L. Goldfarb, M. Gomis, M. Huang, K. Leitzell, E. Lonnoy, J. Matthews, T. Maycock, T. Waterfield, O. Yelekçi, R. Yu, and B. Zhou, Eds. Cambridge, United Kingdom and New York, NY, USA: Cambridge University Press, 2021, pp. 3–32.

[2] United Nations Framework Convention on Climate, "Paris agreement to the united nations framework convention on climate change," 2015.

[3] G. Kuhlmann, G. Broquet, J. Marshall, V. Clément, A. Löscher, Y. Meijer, and D. Brunner, "Detectability of CO_2 emission plumes of cities and power plants with the Copernicus Anthropogenic CO_2 Monitoring (CO2M) mission," *Atmos. Meas. Tech.*, vol. 12, no. 12, pp. 6695–6719, 2019.

[4] J. Strandgren, D. Krutz, J. Wilzewski, C. Paproth, I. Sebastian, K. R. Gurney, J. Liang, A. Roiger, and A. Butz, "Towards spaceborne monitoring of localized CO_2 emissions: An instrument concept and first performance assessment," *Atmos. Meas. Tech.*, vol. 13, no. 6, pp. 2887–2904, 2020.

[5] J. S. Wilzewski, A. Roiger, J. Strandgren, J. Landgraf, D. G. Feist, V. A. Velazco, N. M. Deutscher, I. Morino, H. Ohyama, Y. Té, R. Kivi, T. Warneke, J. Notholt, M. Dubey, R. Sussmann, M. Rettinger, F. Hase, K. Shiomi, and A. Butz, "Spectral sizing of a coarse-spectral-resolution satellite sensor for XCO2," *Atmos. Meas. Tech.*, vol. 13, no. 2, pp. 731–745, 2020.

[6] S. Gimeno García, F. Schreier, G. Lichtenberg, and S. Slijkhuis, "Near infrared nadir retrieval of vertical column densities: Methodology and application to SCIAMACHY," *Atmos. Meas. Tech.*, vol. 4, no. 12, pp. 2633–2657, 2011.

[7] P. Hochstaffl, F. Schreier, G. Lichtenberg, and S. G. García, "Validation of Carbon Monoxide Total Column Retrievals from SCIAMACHY Observations with NDACC/TCCON Ground-Based Measurements," *Remote Sens.*, vol. 10, no. 2, p. 223, 2018.

[8] F. Schreier, S. Gimeno García, P. Hochstaffl, and S. Städt, "Py4CAtS — PYthon for Computational ATmospheric Spectroscopy," *Atmosphere*, vol. 10, no. 5, p. 262, 2019.

[9] P. Hochstaffl, "Trace gas concentration retrieval from short-wave infrared nadir sounding spaceborne spectrometers," Ph.D. dissertation, Ludwig-Maximilians-Universität München, Jan. 2022.

[10] F. Schreier, S. Gimeno García, P. Hedelt, M. Hess, J. Mendrok, M. Vasquez, and J. Xu, "GARLIC – a general purpose atmospheric radiative transfer line-by-line infrared-microwave code: Implementation and evaluation," *J. Quant. Spectrosc. & Radiat. Transfer*, vol. 137, pp. 29–50, 2014.

[11] T. Delahaye, R. Armante, N. A. Scott, N. Jacquinet-Husson, A. Chédin, L. Crépeau, C. Crevoisier, V. Douet, A. Perrin, A. Barbe, V. Boudon, A. Campargue, L. H. Coudert, V. Ebert, J.-M. Flaud, R. R. Gamache, D. Jacquemart, A. Jolly, F. K. Tchana, A. Kyuberis, G. Li, O. M. Lyulin, L. Manceron, S. Mikhailenko, N. Moazzen-Ahmadi, H. S. P. Müller, O. V. Naumenko, A. Nikitin, V. I. Perevalov, C. Richard, E. Starikova, S. A. Tashkun, V. G. Tyuterev, J. V. Auwera, B. Vispoel, A. Yachmenev, and S. Yurchenko, "The 2020 edition of the GEISA spectroscopic database," *J. Mol. Spectrosc.*, vol. 380, p. 111510, 2021.

[12] I. Gordon, L. Rothman, R. Hargreaves, R. Hashemi, E. Karlovets, F. Skinner, E. Conway, C. Hill, R. Kochanov, Y. Tan, P. Wcisło, A. Finenko, K. Nelson, P. Bernath, M. Birk, V. Boudon, A. Campargue, K. Chance, A. Coustenis, B. Drouin, J. Flaud, R. Gamache, J. Hodges, D. Jacquemart, E. Mlawer, A. Nikitin, V. Perevalov, M. Rotger, J. Tennyson, G. Toon, H. Tran, V. Tyuterev, E. Adkins, A. Baker, A. Barbe, E. Canè, A. Császár, A. Dudaryonok, O. Egorov, A. Fleisher, H. Fleurbaey, A. Foltynowicz, T. Furtenbacher, J. Harrison, J. Hartmann, V. Horneman, X. Huang, T. Karman, J. Karns, S. Kassi, I. Kleiner, V. Kofman, F. Kwabia–Tchana, N. Lavrentieva, T. Lee, D. Long, A. Lukashevskaya, O. Lyulin, V.Yu. Makhnev, W. Matt, S. Massie, M. Melosso, S. Mikhailenko, D. Mondelain, H. Müller, O. Naumenko, A. Perrin, O. Polyansky, E. Raddaoui, P. Raston, Z. Reed, M. Rey, C. Richard, R. Tóbiás, I. Sadiek, D. Schwenke, E. Starikova, K. Sung, F. Tamassia, S. Tashkun, J. V. Auwera, I. Vasilenko, A. Vigasin, G. Villanueva, B. Vispoel, G. Wagner, A. Yachmenev, and S. Yurchenko, "The HITRAN2020 molecular spectroscopic database," *J. Quant. Spectrosc. & Radiat. Transfer*, p. 107949, 2021.

[13] G. Anderson, S. Clough, F. Kneizys, J. Chetwynd, and E. Shettle, "AFGL atmospheric constituent profiles (0 - 120 km)," AFGL, Tech. Rep. TR-86-0110, 1986.

[14] D. J. Varon, J. McKeever, D. Jervis, J. D. Maasakkers, S. Pandey, S. Houweling, I. Aben, T. Scarpelli, and D. J. Jacob, "Satellite Discovery of Anomalously Large Methane Point Sources From Oil/Gas Production," *Geophys. Res. Letters*, vol. 46, no. 22, pp. 13 507–13 516, 2019.

[15] D. J. Jacob, D. J. Varon, D. H. Cusworth, P. E. Dennison, C. Frankenberg, R. Gautam, L. Guanter, J. Kelley, J. McKeever, L. E. Ott, B. Poulter, Z. Qu, A. K. Thorpe, J. R. Worden, and R. M. Duren, "Quantifying methane emissions from the global scale down to point sources using satellite observations of atmospheric methane," *Atmos. Chem. Phys.*, vol. 22, no. 14, pp. 9617–9646, Jul. 2022.

[16] S. Jongaramrungruang, C. Frankenberg, G. Matheou, A. K. Thorpe, D. R. Thompson, L. Kuai, and R. M. Duren, "Towards accurate methane point-source quantification from high-resolution 2-D plume imagery," *Atmos. Meas. Tech.*, vol. 12, no. 12, pp. 6667–6681, 2019.